

Synthesis, Characterization and Optoelectronic Properties of Iridium Complexes Bearing Nonconjugated Six-membered Chelating Ligands

*Claus Hierlinger,^{a,b} Amlan K. Pal,^b Filippo Stella,^b Tomas Lebl,^b David B. Cordes,^b Alexandra
M. Z. Slawin,^b Denis Jacquemin^{*c,d} Véronique Guerschais^{*a} Eli Zysman-Colman^{*b}*

^a Institut des Sciences Chimiques de Rennes, UMR 6226 CNRS-Université de Rennes 1,
Campus de Beaulieu, 35042 Rennes Cedex, France. E-mail: veronique.guerchais@univ-
rennes1.fr

^b Organic Semiconductor Centre, EaStCHEM School of Chemistry, University of St
Andrews, St Andrews, Fife, KY16 9ST, UK. E-mail : eli.zysman-colman@st-andrews.ac.uk;
Web: <http://www.zysman-colman.com>

^c UMR CNRS 6230, Université de Nantes, CEISAM, 2 rue de la Houssinière, 44322 Nantes
Cedex 3, France. E-mail: Denis.Jacquemin@univ-nantes.fr

^d Institut Universitaire de France, 1, Rue Descartes, 75005 Paris Cedex 5, France.

Abstract

We report the synthesis, characterization and the optoelectronic properties of a series of four new luminescent iridium(III) complexes **1-4**, of the form $[\text{Ir}(\text{C}^{\wedge}\text{N})_2(\text{N}^{\wedge}\text{N})]\text{PF}_6$ [where $\text{C}^{\wedge}\text{N}$ is the nonconjugated benzyipyridinato (bnpy) and $\text{N}^{\wedge}\text{N}$ is a neutral diimine ancillary ligand] with the goal of investigating the impact of the methylene spacer between the coordination moieties of the $\text{C}^{\wedge}\text{N}$ ligand on the optoelectronic properties of the complexes. The crystal structures of **1-3** illustrate two possible orientations of the methylene unit of the bnpy ligand. The formation of these two separate conformers is a result of the conformational flexibility of the bnpy ligand. In complexes **3** and **4**, mixtures of the two conformers were observed by $^1\text{H-NMR}$ spectroscopy in CDCl_3 at room temperature, whereas only a single conformer is detected for **1** and **2**. Detailed DFT calculations corroborate ROESY experiments, accounting for the presence and relative populations of the two conformers. The optoelectronic properties of all four complexes, rationalized by the theoretical study, demonstrate that the interruption of conjugation in the $\text{C}^{\wedge}\text{N}$ ligands results in a reduced electrochemical gap but similar triplet state energies and lower photoluminescence quantum yields compared to the reference complexes **R1-R4**. Depending on the nature of the $\text{N}^{\wedge}\text{N}$ ligand, we observe (1) marked variations of the ratio of the conformers at ambient temperature and (2) phosphorescence ranging from yellow to red.

Introduction

One of the most promising and explored classes of luminescent transition metal complexes are those based on iridium(III) as they show excellent photo- and thermal stabilities. They are typically highly efficient emitters with relatively short phosphorescent emission lifetimes, and their emission energy can be easily tuned as a function of ligand design.¹⁻² The most widely studied class of iridium complexes are heteroleptic bis-cyclometalated complexes of the form $[\text{Ir}(\text{C}^{\wedge}\text{N})_2(\text{L}^{\wedge}\text{X})]^{n+}$, where $\text{C}^{\wedge}\text{N}$ is the cyclometalating ligand and $\text{L}^{\wedge}\text{X}$ is either a monoanionic ligand such as acetylacetonate (acac, $n = 0$), or a neutral diimine ligand such as

2,2'-bipyridine (bpy, $n = 1$). The main strategies for tuning the emission energy of these complexes are the decoration of the ligands with either electron-withdrawing or electron-donating substituents, and the modification of the coordinating heterocycles.^{1,3-5} The C^N ligands nearly always form *five*-membered chelates, typically based on 2-phenylpyridine (ppyH). Strategies involving interruption of the conjugation in these C^N ligands, such as going from a *five*-membered chelate to a *six*-membered chelate that incorporates a methylene spacer, are far less explored. Indeed, examples of photoactive iridium complexes incorporating *six*-membered chelate C^N ligands remain rare and belong to two categories depending on the presence of conjugated⁶⁻⁸ or nonconjugated⁹⁻¹² bidentate chelating ligands.

To date, to the best of our knowledge, all iridium complexes employing nonconjugated *six*-membered chelate C^N ligands have included either a pyrazole^{9,11} or benzyl-derived *N*-heterocyclic carbene¹⁰ coordinating moiety as part of the ligand. Surprisingly, the use of pyridine, such as with 2-benzylpyridinato (bnpy), has not yet been explored in the design of photoactive iridium complexes; this ligand has only been reported for iridium complexes used in catalysis.¹³⁻¹⁴ The two C^N-coordination moieties in bnpy are separated by a methylene spacer, which fully interrupts the π -conjugation within the C^N ligands. This allows the decoration of the pyridine without influencing the electronic properties of the phenyl ring and therefore the HOMO level of the complex; the HOMO being typically located on the phenyl rings of the C^N ligands and the iridium *d*-orbitals.³ In the present study, we have targeted a series of four new cationic Ir(III) complexes (Chart 1) of the form [Ir(bnpy)₂(N^N)](PF₆), where the N^N ligand is a neutral diimine chelate, with the goal to evaluate whether breaking the conjugation within the C^N ligands can aid in pushing the emission to the blue, which has been an active research theme in the Zysman-Colman group.¹⁵⁻²³ Complexes **1** and **2** contain bipyridine-based ancillary ligands [**1**, N^N = bpy; **2** = 4,4'-di-*tert*-butyl-2,2'-bipyridine (*dtBubpy*)] while complexes **3** and **4** each contain two 5-membered heterocycles in the electron

deficient 2,2'-bithiazole (bthz) and the electron-rich 1*H*,1'*H*-2,2'-biimidazole (biim) ligands, respectively. The motivation for the choice of N[^]N ligands was to have a series of ligands that (1) spanned a wide electronic range and (2) whose bite angles varied in order to assess what impact, if any, this has in conjunction with the C[^]N ligands. The optoelectronic properties of these complexes are explored and compared with benchmark complexes (**R1-R4**, see Chart 1) where the bnpy ligands have been replaced with ppy; **R1-R3** have been previously reported^{15,24} while **R4** is new. The physical and photophysical properties of these complexes are corroborated by density functional theory (DFT) and time-dependent DFT (TD-DFT) investigations.

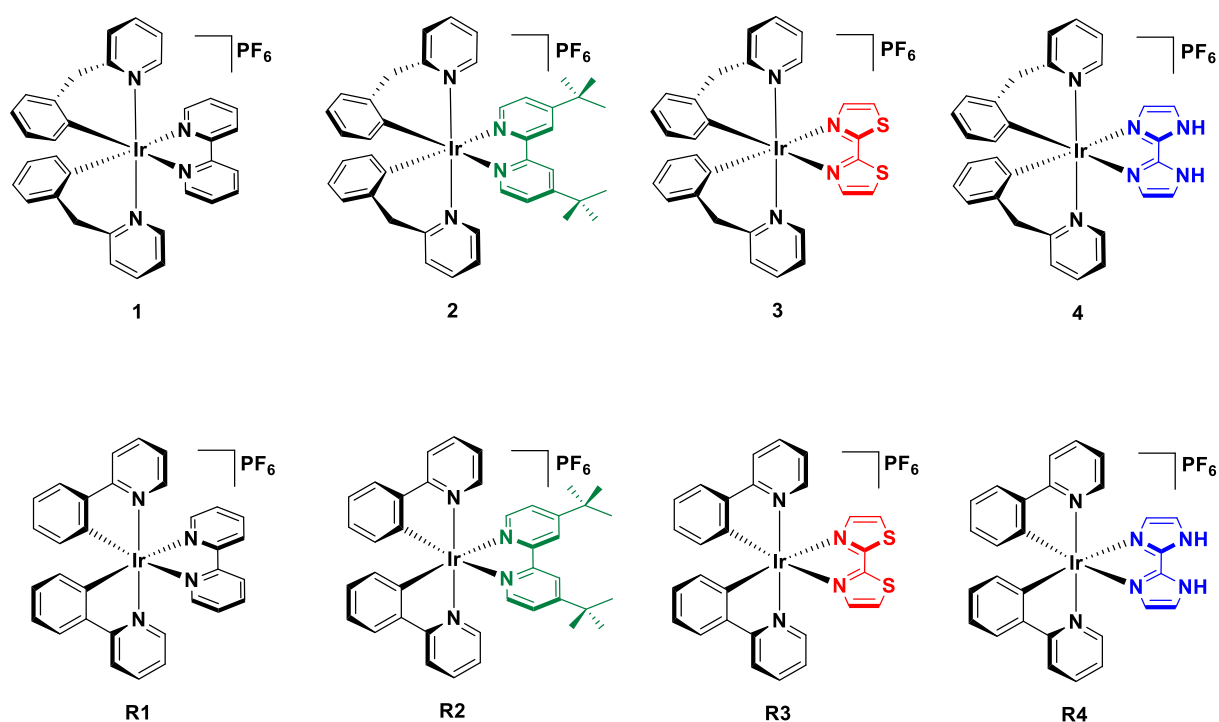


Chart 1. Synthesized and characterized complexes (**1-4**) and reference complexes (**R1-R4**) in this study.

Results and Discussion

Complexes **1-4** were obtained as their hexafluorophosphate salts from the chloro-bridged dimer [Ir(bnpy)₂Cl]₂, upon reaction with the corresponding N[^]N ancillary ligand and

subsequent anion exchange with NH_4PF_6 following standard reaction conditions; complex **R4** was obtained analogously using $[\text{Ir}(\text{ppy})_2\text{Cl}]_2$.²⁵⁻²⁶ In the first step, $[\text{Ir}(\text{bnpy})_2\text{Cl}]_2$ was quantitatively obtained as a yellow solid by treatment of bnpyH with $\text{IrCl}_3 \cdot 6\text{H}_2\text{O}$ in a 3:1 mixture of 2-ethoxyethanol/ H_2O (125 °C, 24 h). This dimer was then cleaved with the appropriate N^N ligand in 1:1 mixture of $\text{CH}_2\text{Cl}_2/\text{MeOH}$ (40 °C, 18 h) to afford the cationic Ir(III) complexes as their chloride salts. After column chromatography on silica (eluent: 5% MeOH in CH_2Cl_2) followed by an ion exchange with aqueous NH_4PF_6 , complexes **1-4** were isolated in excellent yield (78% - 91%) as their hexafluorophosphate salts. The ancillary ligands for **3** (bthz)²⁴ and **4** (biim)²⁰ were obtained according to previous reports. All complexes were characterized by ^1H , ^{13}C and ^{31}P NMR spectroscopy, HR-ESI mass spectrometry, elemental analysis, and melting point determination (see Figures **S1-S19** in the Supporting Information for NMR and HR-ESI-mass spectra). The structures of complexes **1-3** and the chloride salt of **R4**, **R4.Cl**, were determined by single crystal X-ray diffraction.

Crystal Structures

Single crystals of sufficient quality of **1-3** and **R4.Cl** were grown from vapor diffusion of a CH_2Cl_2 or acetone solution of the complex with diethyl ether acting as the anti-solvent. The structures of **1-3** and **R4.Cl** were determined by single-crystal X-ray diffraction (Figure 1, **R4.Cl** is shown in Figure **S20** in the SI). All three (**1-3**) complexes possess a distorted octahedral geometry, with the two bnpy ligands in complexes **1-3** coordinated to iridium to form a six-membered chelate ring. The pyridine rings of the C^N ligand are disposed in a mutually *trans* arrangement while the cyclometalating carbon atoms are *trans* to the nitrogen atoms of the N^N ligand, presenting an analogous binding mode to the majority of cationic Ir(III) complexes such as **R1-R4.Cl**. In **1-3** the Ir- $\text{C}_{\text{C}^{\text{N}}}$ bonds are noticeably shorter [2.022(5) – 2.052(7) Å for **1-3**; 1.988(6) – 2.016(7) for **R4.Cl**] than the Ir- $\text{N}_{\text{N}^{\text{N}}}$ bonds, which range from 2.148(5) to 2.203(4) Å [2.153(5) – 2.184(5) Å for **R4.Cl**]. These bond lengths are all similar to

the analogous bond lengths in **R1-R3**.^{15,24,27-28} The bite angles of the N^N ligands in **1-3** vary from 75.24(15)-77.8(2)° [76.1(2)° for **R4.Cl**], which are again similar to the reference complexes **R1-R3**. The bite angles of the bnpy ligands vary between 87.97(13) and 87.98(13)° for **3**, 88.1(3) and 88.3(6)° for **1**, and 88.8(2) and 89.2(3)° for **2**; reflecting the increasing steric demand of the different N^N ligands. These bite angles are in the same range as those observed in a related complex using a different nonconjugated C^N ligand with a methylene spacer, [Ir(dFbpz)₂(pymbi)]PF₆ [where dFbpzH is 1-(2,4-difluorobenzyl)-1*H*-pyrazole and pymbi 3-methyl-1-(2-pyridyl)-benzimidazolin-2-ylidene-*C,C*²], the bite-angle across the dFbpz ligand being 88.80°.¹¹ As expected, the bite angles of the bnpy ligands are significantly larger than those seen in the reference complexes, which contain five-membered ring C^N chelates [**R1**: 80.00°, **R2**: 80.42°, **R3**: 80.60° and **R4.Cl**: 80.1(3)–80.7(2)°].

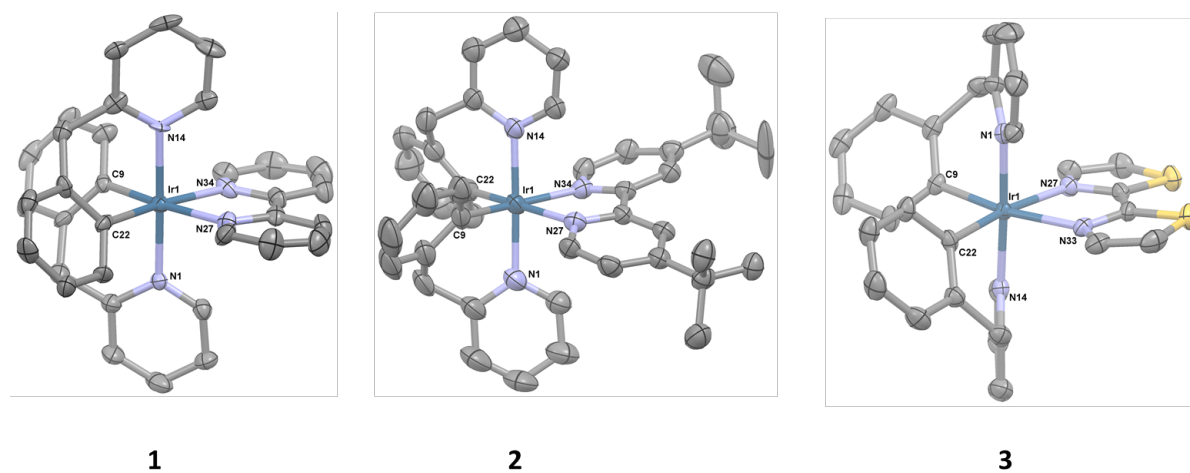


Figure 1. Solid-state structures of complexes **1-3**, with thermal ellipsoids drawn at the 50 % probability level. Hydrogen atoms, PF₆⁻ counterions, solvent molecules and minor components of disorder are omitted for clarity. Note the different orientations of the bnpy ligand in **1** and **2** vs **3**. Color codes are: C = grey, N = light purple, S = yellow and Ir = blue.

In the X-ray structures, the conformation of the bnpy ligands in complexes **1** and **2** differs from that in **3**. Complexes **1** and **2** are found solely as one conformer where the pyridine

rings of the C^N ligand are orientated towards the N^N ligand, whereas, in **3**, the other conformer, where the methylene groups point towards the N^N ligand, is observed, despite this being the minor conformer observed by ¹H NMR (see below). Given the small differences between the conformer free energies computed in solution for **3** (see below), it is not surprising that packing effects can affect the equilibrium and that the most favored conformer differs in solution and in the solid-state. Complex **1** crystallizes in the polar space group *P2*₁, so individual crystals could be enantiopure, resulting from conglomerate crystallization; however the Flack parameter [0.305(7)] indicates the likelihood of individually racemic crystals being present. Complexes **2** and **3** crystallize in centrosymmetric space groups (*P* $\bar{3}$ and *P* $\bar{1}$, respectively), so exist as racemates in the crystalline state.

Solution-State NMR studies

The room temperature ¹H NMR spectra in CDCl₃ of **1-4** are depicted in Figure 2. Complexes **1** and **2** each show one set of two doublets in the region of $\delta = 4.80 - 3.30$ ppm, corresponding to the diastereotopic methylene protons of the C^N ligand, the result of magnetic nonequivalence imparted by the proximal iridium stereocenter. By contrast, there are two sets of two doublets with an integration ratio of 1:1.2 in the same region of ¹H NMR spectrum of **3**. Furthermore, two sets of aromatic signals are also apparent, which implies the presence of two conformers (designed as a and b, see below) in solution. Two conformers, in a ratio of 1:0.2 for conformer a:conformer b, are also present in **4** as observed by ¹H NMR. This phenomenon was previously reported in related neutral Ir(III) complexes containing 1-(2,4-difluorobenzyl)-1*H*-pyrazole (dFbpzH) as the C^N ligands and was associated with restricted conformational flexibility of six membered C^N chelates.⁹

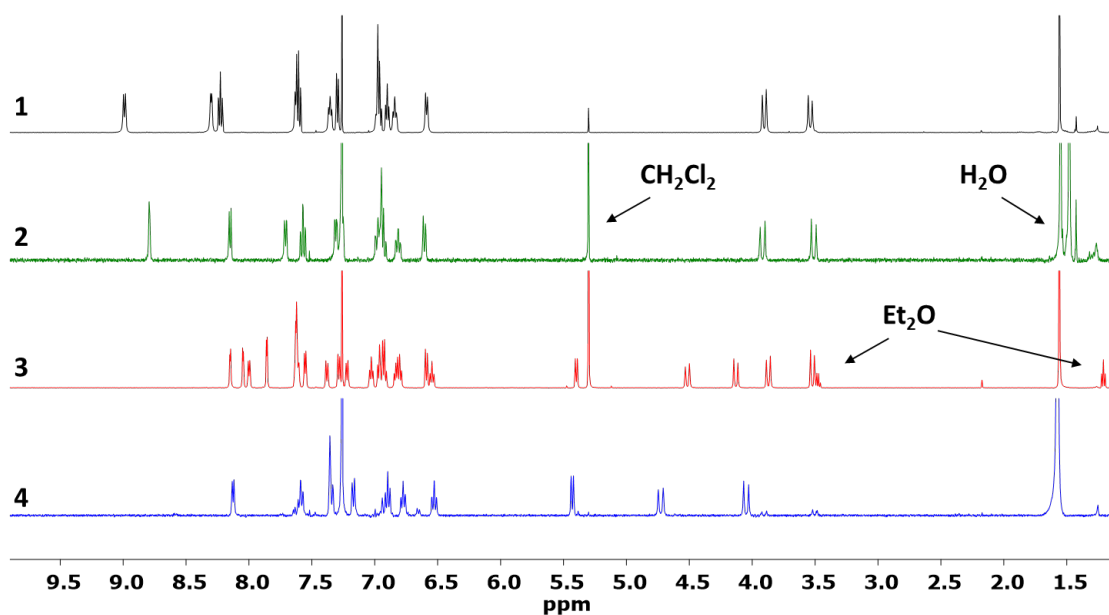


Figure 2. Room-temperature ^1H -NMR spectra of complexes **1-4** in CDCl_3 .

This presence of two conformers prompted us to perform DFT calculations (see the Supporting Information for more details). For each of the complexes, we could optimize stable structures for both conformers, differing in orientation of the methylene bridge of the $\text{C}^{\wedge}\text{N}$ ligand, as shown in Figure 3 for complex **3** (see Figure S21 the SI for **4**). The conformer **3a** has the same orientation of the methylene bridge as found in the solid state by X-ray crystallography, whereas the geometry of **3b** is analogous to those found in the crystal structures of **1** and **2** (see above). For all compounds, both conformers belong to the C_2 point group. Given that DFT calculations have been performed in MeCN solution, the DFT-determined bond lengths reasonably match their experimental counterparts, *e.g.*, the Ir- $\text{C}^{\wedge}\text{N}$ bonds are 2.02 Å long by DFT and 2.022(5) – 2.052(7) Å for **1-3** long in the X-ray, whereas the Ir- $\text{N}^{\wedge}\text{C}$ distances are 2.10 Å according to the calculation and 2.069(4) – 2.098(11) Å for **1-3** in the solid-state structure.

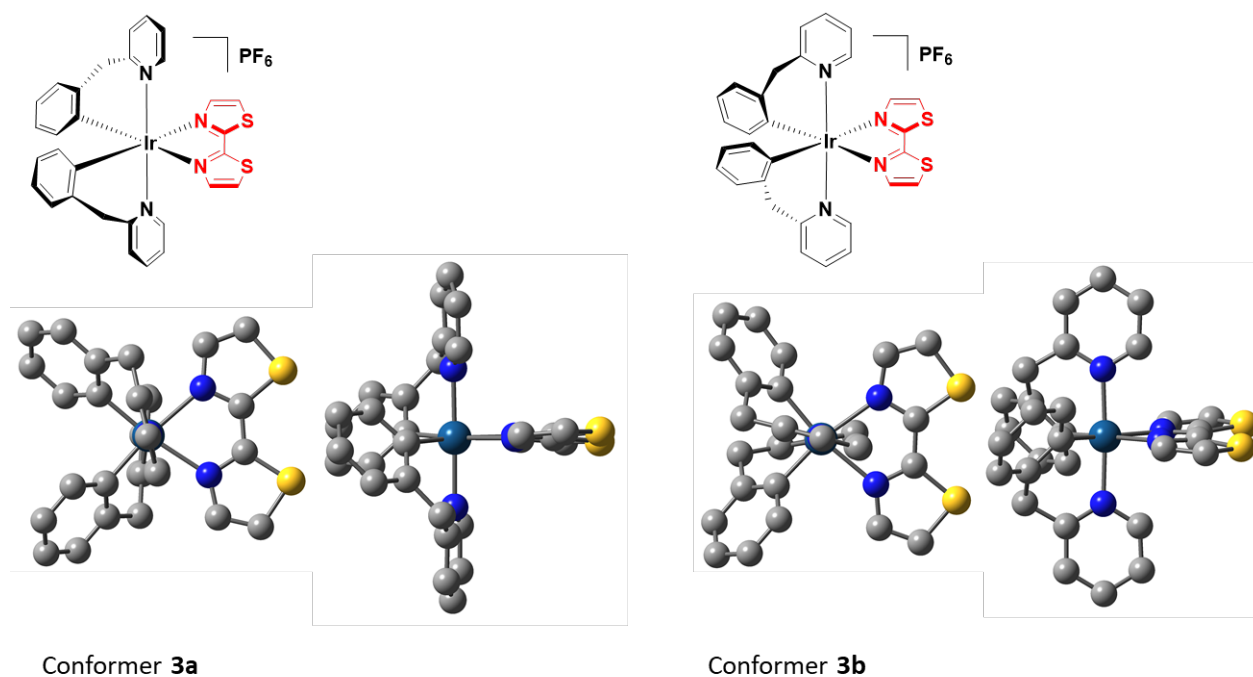


Figure 3. DFT-optimized geometry of conformers **3a** (left) and **3b** (right). Hydrogen atoms are omitted for clarity.

The chemical exchange cross-peaks (red highlighted) in the 2D ROESY spectrum indicate the existence of a dynamic equilibrium between conformers **3a** and **3b** in solution (Figure 4). Furthermore, the ROESY enables assignment of ^1H resonances to each of the conformers. The NOE cross-peak (blue highlighted) between doublets at 4.54 and 8.18 ppm is only possible for conformer **3a** that has one proton of methylene bridge close (2.56 Å according to DFT) to the aromatic proton of the N[^]N ligand (Figure 3). By contrast, this NOE enhancement is not observed for conformer **3b** due to a longer distance between the methylene bridge and the N[^]N ligand (5.12 Å according to DFT).

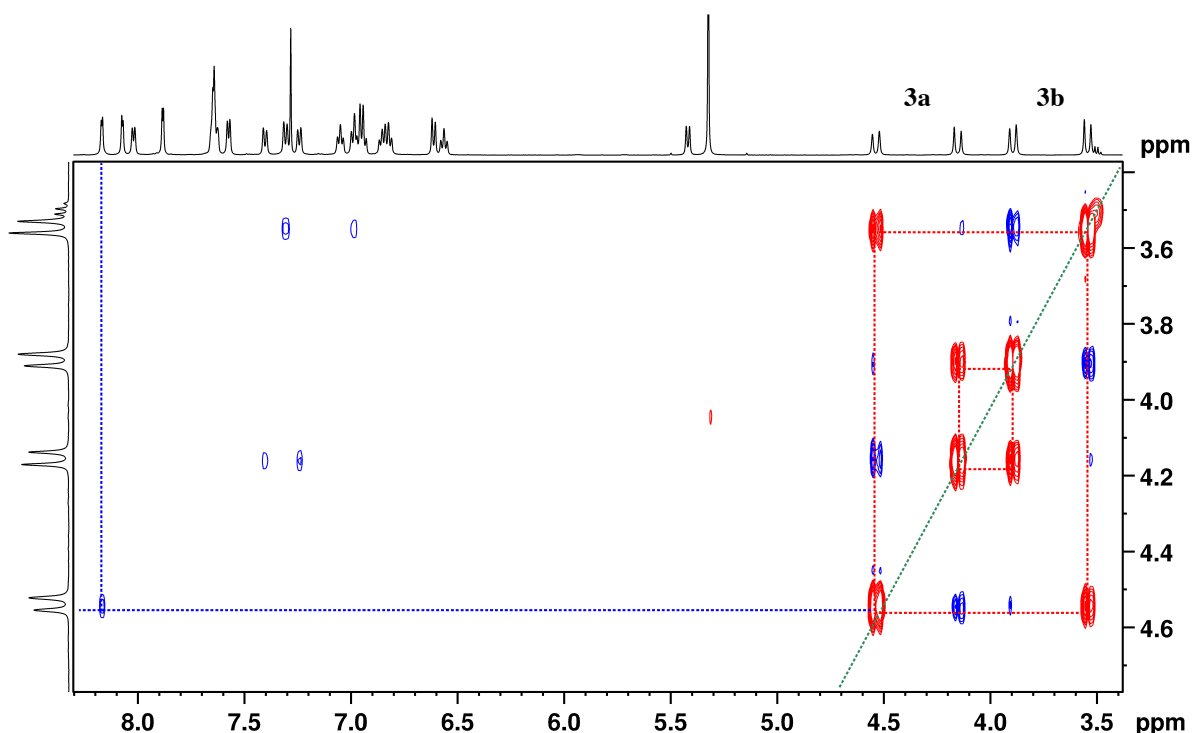


Figure 4. 2D ROESY spectrum of **3** in CDCl_3 at room temperature. The blue and red cross-peaks indicate magnetization transfer due to NOE and chemical exchange, respectively. The cross-peak between doublets at 4.54 and 8.18 ppm enables assignment of those resonances to conformer **3a**.

DFT computed relative free energies and theoretical Boltzmann distribution can be found in Table 1. As can be seen, there is a remarkable agreement between the ratio of the two conformers determined by theory and experimentally from the relative integral intensities of methylene group ^1H resonances (Table 1). There seems to be a global trend that the steric stress, that decreases in the $1 \sim 2 > 3 > 4$ series, makes conformer a more accessible in the latter compounds (**3a** and **4a**) than in the former (**1a** and **2a**). The DFT determined distances between the (closest) hydrogen atoms of the methylene and $\text{N}^{\wedge}\text{N}$ ligand are: 2.15, 2.14, 2.23 and 2.28 Å, in **1a**, **2a**, **3a** and **4a**, respectively. For **3**, we attempted to optimize by DFT a mixed conformer with one of the ligands in each conformation, but this induces a steric clash and the optimization process led back to one of the two conformers. This clearly suggests that the

transition from one conformation to the other should be a concerted process in which the two ligands simultaneously change their conformation. We therefore searched for the corresponding transition state, and we could locate it $66 \text{ kJ}\cdot\text{mol}^{-1}$ above the most stable **3b** structure on the free energy scale. This indicates that while thermal equilibration between the two conformers is attainable at room temperature, the interconversion will not be rapid, which is consistent with the fact that two separate sets of signals could be detected on the NMR timescale. The corresponding imaginary frequency mode at 40.5 i cm^{-1} is given in the SI (see video **S1**).

The interconversion of conformers **3a** and **3b** was also studied by variable temperature NMR spectroscopy from 280 to 315 K. The variable-temperature ^1H NMR studies showed considerable dependence of equilibrium constant, K , on the temperature (Figure **S22**). Analysis of the Van't Hoff plot yielded the following thermodynamic parameters $\Delta G^\circ_{298} = -0.63 \pm 0.05 \text{ kJ}\cdot\text{mol}^{-1}$, $\Delta H^\circ = 7.3 \pm 0.4 \text{ kJ}\cdot\text{mol}^{-1}$ and $\Delta S^\circ = 26.6 \pm 1.5 \text{ J}\cdot\text{mol}^{-1}\cdot\text{K}^{-1}$, indicating that at 298 K **3b** is moderately more stable than **3a**. The rate constants of interconversion between the two conformers were derived from the intensity of the exchange cross peaks in the ROESY spectra (Figure **S23**). The corresponding activation parameters determined from an Eyring analysis are summarized in Table 2. The activation energy obtained experimentally for **3b** to **3a** ($72.2 \pm 3.2 \text{ kJ}\cdot\text{mol}^{-1}$) is in very good agreement with the DFT calculation ($66.6 \text{ kJ}\cdot\text{mol}^{-1}$). Surprisingly both Eyring and Van't Hoff plot analysis suggest large positive entropy for the isomerization of **3a** to **3b**. These significant entropic changes were not reproduced by DFT calculations, but we note that the entropic term is the most approximated thermodynamic term in the traditional DFT calculations of total and reaction (free) energies.

Table 1. Comparison of relative DFT Gibbs energies of the conformers **1b** - **4b** with respect to conformers **1a** - **4a**, respectively (ΔG°), Boltzmann ratio, corresponding equilibrium constant,

K, at 298 K and ratio of conformers derived from relative integral intensities of methylene group ^1H resonances.

	1	2	3	4
$\Delta G^\circ / \text{kJ}\cdot\text{mol}^{-1}$	-13.4	-9.6	-2.1	5.4
Boltzmann ratio (a:b)	0.004:1	0.02:1	0.43:1	1:0.11
K	223	48.2	2.33	0.113
Ratio of conformers a:b	0:1	0:1	0.83:1	1:0.17

Table 2. Activation parameters for the interconversion between conformers **3a** and **3b** for complex **3** obtained by Eyring plot analysis of the rate constants for conformer interconversion at various temperatures.

Conformer	$\Delta G_{298\text{K}}^\ddagger$ / $\text{kJ}\cdot\text{mol}^{-1}$	ΔH^\ddagger / $\text{kJ}\cdot\text{mol}^{-1}$	ΔS^\ddagger / $\text{J}\cdot\text{mol}^{-1}\cdot\text{K}^{-1}$
3a	70.6 ± 4.9	80.0 ± 2.4	31.6 ± 8.1
3b	72.2 ± 3.2	71.9 ± 1.6	-0.8 ± 5.5

Electrochemical properties

The electrochemical behavior for **1-4** and **R4** was evaluated by cyclic voltammetry (CV) and differential pulse voltammetry (DPV) in deaerated MeCN solution containing $n\text{-Bu}_4\text{NPF}_6$ as the supporting electrolyte and ferrocene/ferrocenium (Fc/Fc^+) as the internal reference. The potentials are referenced with respect to SCE ($\text{Fc}/\text{Fc}^+ = 0.38\text{ V}$ in MeCN)²⁹ at 298 K. The electrochemistry data, obtained at a scan rate of 100 mV s^{-1} , can be found in Table 3 (including data from **R1-R4**) and the voltammograms are shown in Figure 5 (**R4** is shown in Figure S24 in the SI). All complexes show a quasi-reversible single electron oxidation peak, which is attributed to the Ir(III)/Ir(IV) redox couple with contributions from the phenyl rings of the bnpv. Throughout the series, complexes **1-4** are easier to oxidize than their corresponding reference complexes **R1-R4** with cathodic shifts ranging from 0.09 to 0.40 V as the result of the interruption of the π -conjugation. The absence of a conjugated coordinating pyridine results in

a destabilized HOMO, compared to the analogous ppy reference complexes; for instance, according to DFT the HOMO is 0.24 eV lower in **R1** than in **1** (see Figure **S25**). For instance, the oxidation potential of **1** at 1.12 V is significantly shifted to less positive potential than that of **R1** ($E_{1/2}^{ox} = 1.27$ V).¹⁵ A more dramatic cathodic shift of 400 mV is observed for **2** ($E_{1/2}^{ox} = 0.91$ V) compared to **R2** ($E_{1/2}^{ox} = 1.31$ V).¹⁶ The oxidation potential of **3** at 1.15 V is similar to **1** and, likewise is easier to oxidize than **R3** ($E_{1/2}^{ox} = 1.24$ V).²⁴ The oxidation potential of **4** at 1.05 is modestly cathodically shifted by 7 mV compared to **1** and by 10 mV compared to **R4** ($E_{1/2}^{ox} = 1.15$ V). The cathodic shifting of the complexes **2** and **4** compared to that of **1** reflect the more electron-rich nature of the ancillary ligand, which serves to modulate the electronics of the iridium center.

Complexes **1-3** show monoelectronic reversible first reduction waves, reflecting a reduction of the ancillary ligand in each case. No reduction wave was detected for **4**, a feature also found for related biim-containing cationic Ir(III) complexes such as [(dFppy)₂Ir(biim)](PF₆) (where dFppy = 2-(2,4-difluorophenyl)pyridinato).²⁰ The voltammograms for **R4** however show two irreversible reduction waves at -1.95 V and -2.29 V. The reversible reduction potentials for **1-3** are in a similar range to those of **R1-R3** and other related cationic Ir(III) complexes where N[^]N-based reduction is well-documented.³⁰ The reduction potential of **1** at -1.38 V is the same as that found for **R1**.¹⁵ Complex **2**, bearing the electron-rich dtBubpy N[^]N ligand, is more difficult to reduce than **1**, with $E_{1/2}^{red} = -1.58$ V. This reduction potential is significantly cathodically shifted however compared to **R2** ($E_{1/2}^{red} = -1.40$ V). In contrast the reduction potential for **3** is shifted anodically by 270 mV to -1.11 V compared to **1**, which is similar to that of **R3** ($E_{1/2}^{red} = -1.15$ V).²⁴ A second, irreversible reduction wave at -1.81 V is observed for **3**, also present in the voltammogram of **R3**.

In acetonitrile, the DFT-computed HOMO levels in acetonitrile of the major conformer of complexes **1-4** are -5.67 eV (**1b**), -5.63 eV (**2b**), -5.69 eV (**3b**), -5.74 eV (**4a**), respectively. The HOMO levels inferred from the CV data are systematically slightly higher in energy compared to the DFT data at -5.54 eV (**1**), -5.33 eV (**2**), -5.57 eV (**3**) and -5.47 eV (**4**). A notable destabilization of the experimentally determined HOMO of **1** and **2** is observed compared to their respective reference complexes **R1** (-6.07 eV) and **R2** (-6.11 eV); the same trend is found but is less pronounced when comparing the HOMO energies of **3** and **4** to **R3** (-5.85 eV) and **R4** (-5.57 eV). This destabilization is consistent with the interruption of the electronic communication between the phenyl ring and the electron-withdrawing pyridine in the C^N ligands.

The DFT computed LUMO energies in acetonitrile of **1-4** are -2.42 eV (**1b**), -2.23 eV (**2b**) and -2.82 eV (**3b**); the calculated LUMO energy for **4a** is -1.59 eV. The LUMO levels for **1-3** could be straightforwardly estimated from the CV data and the experimental results are in line with the computed trends. The experimentally inferred LUMO of **2** ($E_{\text{LUMO}} = -2.84$ eV) is destabilized compared to **1** ($E_{\text{LUMO}} = -3.04$ eV) as a result of the presence of the electron-donating *t*-butyl substituents on the N^N ligand. This effect is more pronounced than that observed between **R1** and **R2** ($E_{\text{LUMO}} = -3.42$ eV and -3.40 eV, respectively). The presence of the strongly π -accepting bithiazole N^N ligand in **3** leads to a significant stabilization of the LUMO ($E_{\text{LUMO}} = -3.31$ eV) compared to those of **1** and **2**. Complex **3**, however, exhibits a more stabilized LUMO level ($E_{\text{LUMO}} = -3.31$ eV) than **R3** ($E_{\text{LUMO}} = -2.76$ eV). The HOMO-LUMO gap of complexes **1** and **2** (experiment: 2.50 and 2.49 eV, theory: 3.25 and 3.40 eV for **1** and **2**, respectively) are larger than that of **3** (experiment 2.26 eV, theory: 2.87 eV) but are all smaller

compared to their reference complexes **R1-R3** (experiment 2.65, 2.71 and 2.39 eV, respectively).

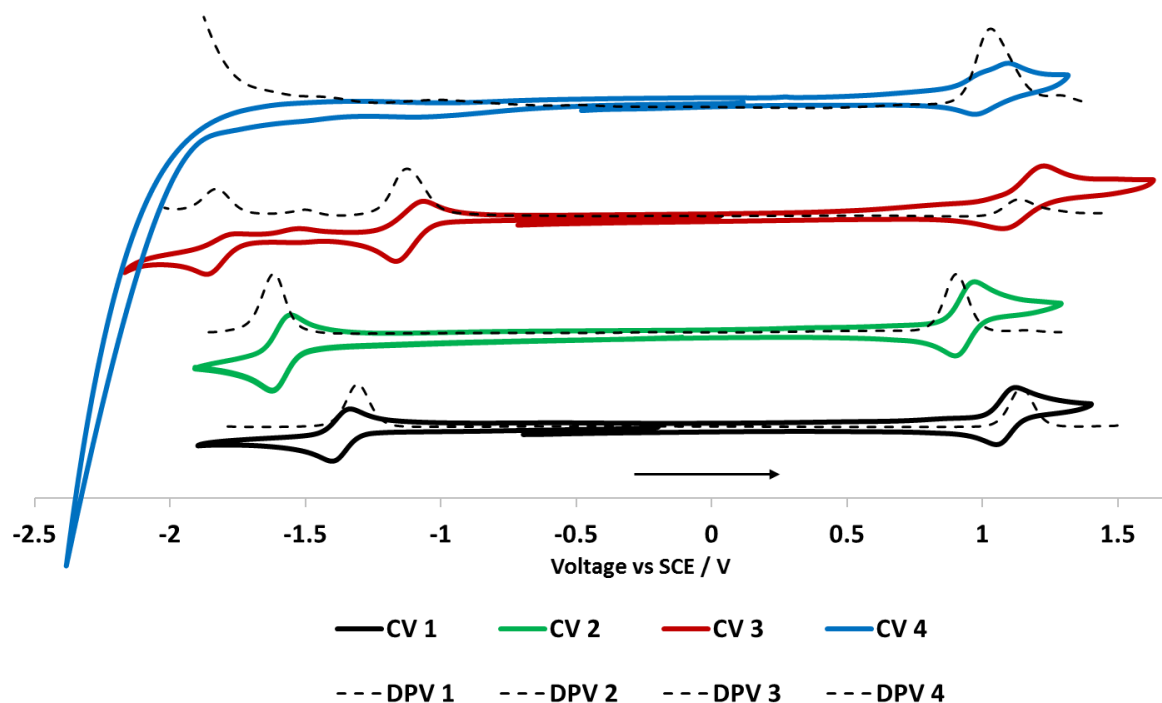


Figure 5. Cyclic voltammograms (in solid lines) and differential pulse voltammetry (in dotted lines) for **1-4** carried out in degassed MeCN at a scan rate of 100 mV s^{-1} , with Fc/Fc^+ as the internal reference, referenced to SCE (0.38 V vs. SCE).²⁹

Table 3. Electrochemical properties of **1-4** and **R1-R4**

Electrochemistry ^a							
	$E_{1/2}^{ox} / \text{V}$	$\Delta E_p / \text{mV}$	$E_{1/2}^{red} / \text{V}$	$\Delta E_p / \text{mV}$	$\Delta E_{redox}^b / \text{V}$	E_{HOMO}^c / eV	E_{LUMO}^c / eV
1	1.12	78	-1.38	74	2.50	-5.54	-3.04
2	0.91	75	-1.58	77	2.49	-5.33	-2.84
3	1.15	140	-1.11, -1.81 ^d	80	2.26	-5.57	-3.31
4	1.05	75	n.d. ^e	-	-	-5.47	-
R1^f	1.27	56	-1.38	55	2.65	-6.07	-3.42
R2^f	1.31	106	-1.40	87	2.71	-6.11	-3.4

R3^g	1.24	-	-1.15	-	2.39	-5.85	-2.76
R4	1.15	91	-1.95, ^d	-	3.10	-5.57	-2.47
			-2.29 ^d				

^a in degassed MeCN at a scan rate of 100 mV s⁻¹ with Fc/Fc⁺ as internal reference, and referenced with respect to SCE (Fc/Fc⁺ = 0.38 V in MeCN);²⁹ ^b ΔE_{redox} is the difference (V) between first oxidation and first reduction potentials; ^c $E_{\text{HOMO/LUMO}} = -[E^{\text{ox/red}} \text{ vs Fc/Fc}^+ + 4.8] \text{ eV}$;³¹ ^d irreversible; ^e not detectable in MeCN; ^f from ref ¹⁵; ^g from ref ²⁴.

Photophysical properties

The UV-Visible absorption spectra of **1-4**, recorded in MeCN at 298 K, are shown in Figure 6 and the data are summarized in Table S2; the spectrum of **R4** is shown in Figure S26 in the SI. All complexes show intense high-energy (ϵ on the order of $2.0\text{-}3.5 \times 10^4 \text{ M}^{-1} \text{ cm}^{-1}$) absorption bands below 280 nm that are attributed to $^1\pi\text{-}\pi^*$ ligand-centered (^1LC) transitions localized on the ancillary ligand, analogous to the corresponding bands found for their reference complexes **R1-R4**.^{15,24} The UV-vis spectrum of **3** is dominated by a moderately intense energy band at 322 nm ($\epsilon = 1.7 \times 10^4 \text{ M}^{-1} \text{ cm}^{-1}$) and a second less intense band at 374 nm ($\epsilon = 0.5 \times 10^4 \text{ M}^{-1} \text{ cm}^{-1}$). This absorption profile is similar to that for **R3**²⁴ and those observed in related systems containing thiazole-based ancillary ligands.³²⁻³³ Complex **4** shows moderately intense bands at 386 nm ($\epsilon = 0.4 \times 10^4 \text{ M}^{-1} \text{ cm}^{-1}$), which are also present in both **R4** and $[\text{Ir}(\text{dFppy})_2(\text{biim})]^+$.²⁰ Similar to the bands observed for **R1-R4**, **1-4** show weak bands (ϵ on the order of $10^3 \text{ M}^{-1} \text{ cm}^{-1}$) in the region of 440-490 nm and tailing to 550 nm. To probe the nature of the low-lying transitions in these complexes, we have used TD-DFT. For **1**, the TD-M06 calculations yield the four lowest singlet excited-states at 534 nm ($f=0.003$), 426 nm ($f=0.002$), 413 nm ($f=0.010$) and 399 nm ($f=0.083$). The former corresponds to a HOMO to LUMO transition (see Figure 7) and can therefore be ascribed to a CT from the phenyl rings of the C[^]N ligand and the metal atom to the bipyridine. The second involves a HOMO-2 to LUMO transition and is clearly MLCT. The third is a HOMO-1 to LUMO+1 transition and can

therefore be characterized as mainly an ILCT, the electronic density moving from the phenyl (and in part the metal) to the pyridyl rings of the C^N ligands. The fourth transition is characterized by HOMO-1 to LUMO character and is also CT in nature, similar to the first band. For the **R1** molecule, the two lowest TD-DFT singlets are located at 483 nm ($f=0.0004$) and 404 nm ($f=0.064$). In **R1**, the HOMO and LUMO have the same electronic distribution as in **1**, but both HOMO-1 and LUMO+1 are more delocalized than in **1** (see Figure S25 in the SI), which is the consequence of breaking of the π -conjugation due to the methylene unit. For **2**, the four lowest singlet excited-states are calculated at 500 nm ($f=0.003$), 415 nm ($f=0.008$), 406 nm ($f=0.007$) and 385 nm ($f=0.098$). There is therefore a moderate hypsochromic displacement of the transitions between the ground state and the first, second and fourth singlet excited states as a consequence of the presence of the more electron-rich dtBubpy N^N ligand in **2**, and a smaller shift for the third state, which is itself consistent with the fact that this transition does not involve the bipyridine in **1** nor in **2**. Indeed, the nature of the states and the shapes of the orbitals in **2** are essentially unchanged compared to **1**. In **3**, the four lowest-lying singlet excited-states are at 638 nm ($f=0.002$), 486 nm ($f=0.002$), 443 nm ($f=0.096$) and 413 nm ($f=0.014$), and they mainly correspond to HOMO to LUMO, HOMO-2 to LUMO, HOMO-1 to LUMO and HOMO to LUMO+1 transitions, respectively. In **3**, the strongest low-lying transition is therefore significantly bathochromically shifted compared to **1**, which fits experimental trends (Figure 6). The frontier MOs of **3b** are displayed in Figure S27 in the SI and the same nature as in **1** is found but for the LUMO+2 that is centered on the pyridyl of the C^N ligand in **3** rather than ancillary ligand in **1**. In **4**, TD-DFT locates the lowest singlet states at higher energy than in **1-3**: 392 nm ($f=0.001$, HOMO-LUMO), 380 nm ($f=0.001$, HOMO-LUMO+1), 359 nm ($f=0.007$, HOMO-LUMO+2) and 353 nm ($f=0.165$, HOMO-1-LUMO+1). The topology of the MOs of **4b** are displayed in Figure S28 in the SI and it is notable that the LUMO and LUMO+1 are inverted compared to **3**, but the nature of the most intense low-lying intense CT band is conserved.

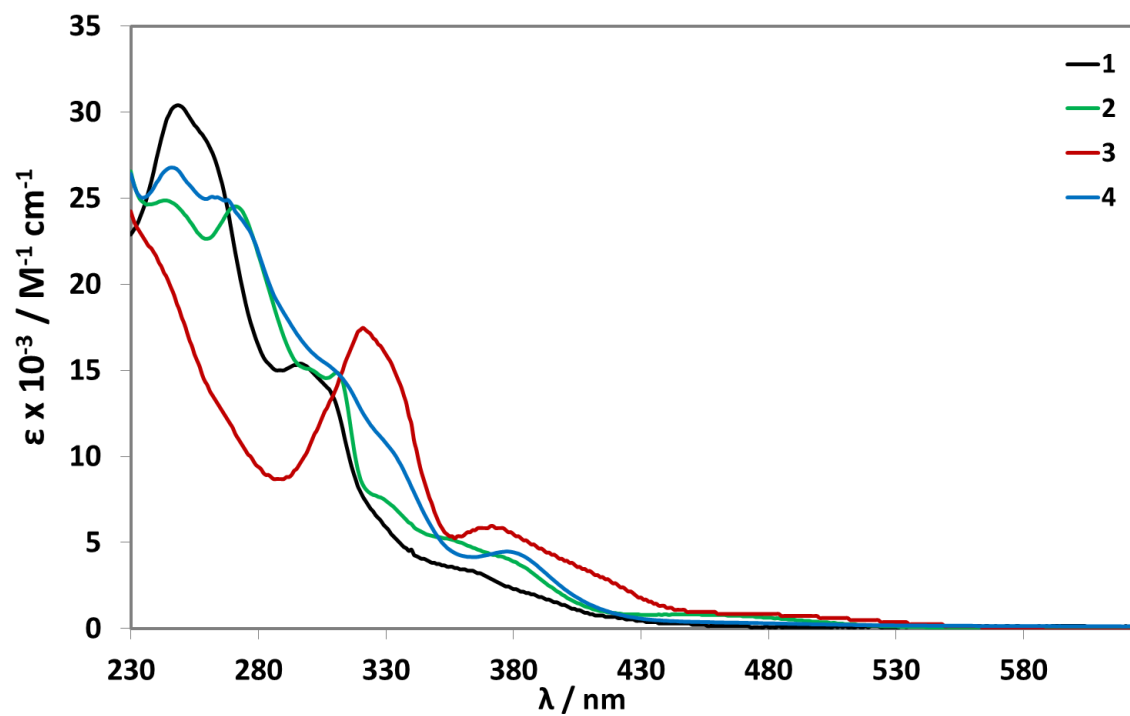


Figure 6. UV-vis absorption spectra in MeCN at 298 K of complexes 1-4.

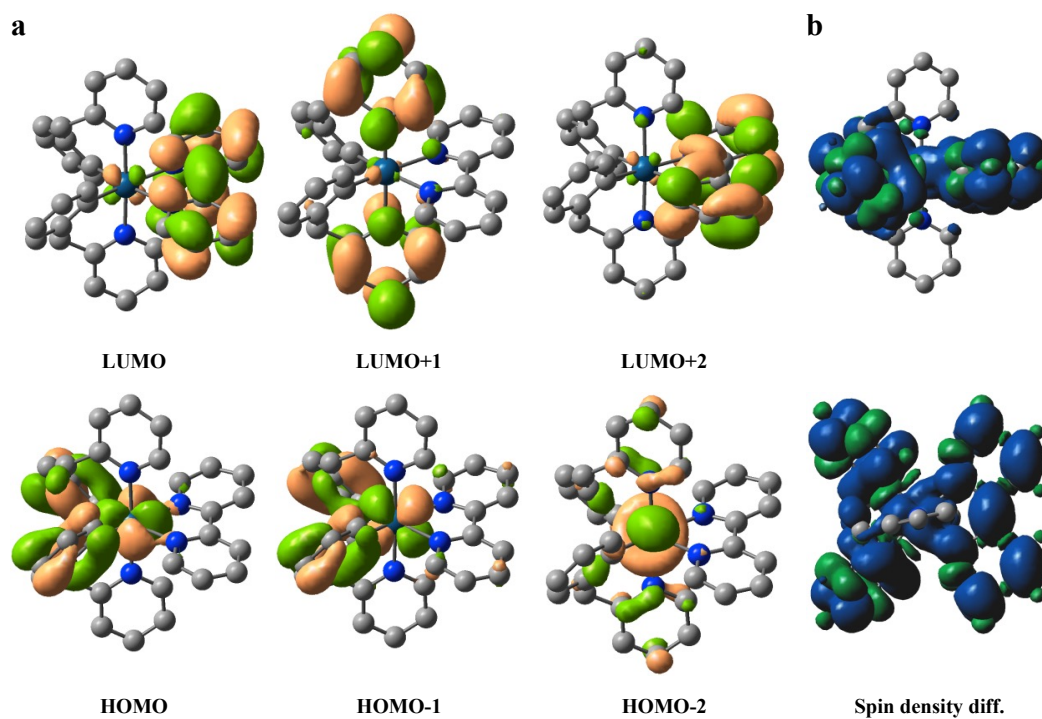


Figure 7. a) Representation of the Kohn-Sham molecular orbitals for **1**. b) spin density difference of the lowest triplet state in its optimal geometry (two views).

The photoluminescence properties of **1-4** were investigated at 298 K in degassed MeCN and in polymethyl methacrylate (PMMA) doped films (5 wt% of complex in PMMA). The spectra are shown in Figure **8a**, whereas Figure **8b** shows the spectra in 2-methyltetrahydrofuran (2-MeTHF) glass at 77 K. The photophysical data of **1-4** and **R1-R4** are summarized in Table **4**. The emission spectrum of **R4** in degassed MeCN is shown in Figure **S29** in the SI. Upon photoexcitation ($\lambda_{\text{exc}} = 420$ nm for **1-3** and 400 nm for **4**) each of the emission profiles observed at room temperature is broad and unstructured, which is consistent with an emission from a mixed MLCT/LLCT state (Figure **7b**), similar in character to that observed for **R1-R3**^{24,34} and **R4**. In solution, the emission maxima are ordered from 580, 585, 602 and 655 nm for **4, 2, 1** and **3**, respectively. The emission energy of **1** is the same as that for **R1** ($\lambda_{\text{PL}} = 602$ nm in MeCN).¹⁵ Complexes **2** and **3** are very slightly shifted (6 nm, 174 cm^{-1} , and 3 nm, 70 cm^{-1}) compared to **R2** and **R3** ($\lambda_{\text{em}} = 591$ nm in MeCN¹⁵ and $\lambda_{\text{em}} = 658$ nm in MeCN).²⁴ Comparing **4** to **R4** ($\lambda_{\text{PL}} = 489$ nm) a much larger shift of 91 nm (3209 cm^{-1}) is observed.

The photoluminescence quantum yields in MeCN ($\Phi_{\text{PL, MeCN}}$) for **1-4** are low (<10%) and each complex shows a Φ_{PL} that is reduced compared to the corresponding reference complexes, except complex **3**. For instance, the $\Phi_{\text{PL, MeCN}}$ for **1** and **2**, at 3% and 8%, are lower than that of **R1** and **R2**, at 9% and 27%, respectively.¹⁵ The $\Phi_{\text{PL, MeCN}}$ for **3** is 3%, which is similar to that for **R3** (2%).²⁴ Complex **4** is very weakly emissive with a $\Phi_{\text{PL, MeCN}}$ smaller than 1%, significantly lower than its **R4** counterpart ($\Phi_{\text{PL, MeCN}} = 66\%$), showing the deleterious effect of the bnpy ligand in this case. Note that **4** is the only complex in the series for which conformer **a** is the most stable in the ground electronic state at room temperature, and this

specific arrangement has an influence on the resulting photophysical properties as shown by DFT studies (see below).

The increased conformational flexibility of the C^N ligands is the likely culprit for the reduced Φ_{PL} values in **1-4** compared to **R1-R4**. To gain more insights, we performed DFT optimizations of the lowest triplet excited-states. We computed a 0-0 phosphorescence wavelength of 654 nm, 620 nm, 793 nm and 510 nm for **1**, **2**, **3** and **4**, respectively. Despite the obvious fact that the absolute DFT values do not perfectly match the experimental values (ca. 0.22 eV average error compared to the λ_{PL} maxima in solution), we note that the theoretical **4** < **2** < **1** < **3** ranking does match the experimental trend. More importantly, in the triplet state, DFT predicts that conformer b is always the most stable, even for **4**. This suggests that, after intersystem crossing, which is generally very efficient in Ir-complexes, **4** might change conformation before phosphorescence takes place, which would obviously be detrimental for the photoluminescence quantum yield. In turn, this might explain why **4** is the poorest emitter of the series.

Complexes **1-4** all exhibit a three-component decay in the sub-microsecond regime (*cf.* Table 4). The weighted average lifetimes, τ_{PL} , for **1-4** are 124, 275, 71 and 235 ns, respectively, and are shorter compared to their reference complexes ($\tau_{\text{PL}} = 275, 386, 81, 852$ ns for **R1-R3**^{15,24} and **R4**, respectively). From these values, radiative and non-radiative rate constants in MeCN can be estimated. The radiative rate constants, k_r , for **1** ($2.41 \times 10^5 \text{ s}^{-1}$) and **2** ($2.91 \times 10^5 \text{ s}^{-1}$) are similar and much larger than that for **4** with $k_r = 0.21 \times 10^5 \text{ s}^{-1}$. These complexes (**1**, **2** and **4**) all possess much smaller k_r than their reference complexes (**R1**, **R2** and **R4**). Complex **3** shows the highest radiative rate constant with $k_r = 4.2 \times 10^5 \text{ s}^{-1}$, which is also higher than **R3** ($k_r = 2.12 \times 10^5 \text{ s}^{-1}$). However, complex **3** also shows the highest non-radiative rate constant k_{nr} value ($135.95 \times 10^5 \text{ s}^{-1}$), and which is slightly higher than the value of **R3** ($k_{\text{nr}} = 121.33 \times 10^5 \text{ s}^{-1}$). Complex **1**

($k_{nr} = 77.97 \times 10^5 \text{ s}^{-1}$) shows a higher k_{nr} than **2** ($33.49 \times 10^5 \text{ s}^{-1}$), which can be explained in part by the red-shifted emission of **1** compared to that of **2**. Compared to their reference complexes, both **1** and **2** show much higher k_{nr} values ($k_{nr} = 33 \times 10^5 \text{ s}^{-1}$ for **R1** and $k_{nr} = 19 \times 10^5 \text{ s}^{-1}$ for **R2**). The poorly emissive complex **4** possesses a k_{nr} of $42.43 \times 10^5 \text{ s}^{-1}$, which is much higher than the value for **R4** ($3.99 \times 10^5 \text{ s}^{-1}$).

The emission energies in PMMA-doped films (5 wt% of complex in PMMA) are not significantly changed compared from those in MeCN. The emission maxima in **1-3** remain essentially unchanged whereas complex **4** shows a modest blue shift of 15 nm (458 cm^{-1}) in the film. The photoluminescence quantum yields of the films ($\Phi_{PL, PMMA}$) are expectedly significantly increased compared to the solution-state measurements and range from 1% (for **4**) to 7% (for **3**) to 15% (**1**) to 21% (**2**). The increase in Φ_{PL} in the doped films is attributed mainly to a reduction in k_{nr} due to the expected limitations of the conformational motion of the C^N ligands. Each of **1-4** in doped films exhibit a three-component emission decay in the sub-microsecond regime. The weighted average lifetimes for **1-4** are 404, 509, 323 and 1196 ns, respectively, which are on average longer than in those measured in solution-state.

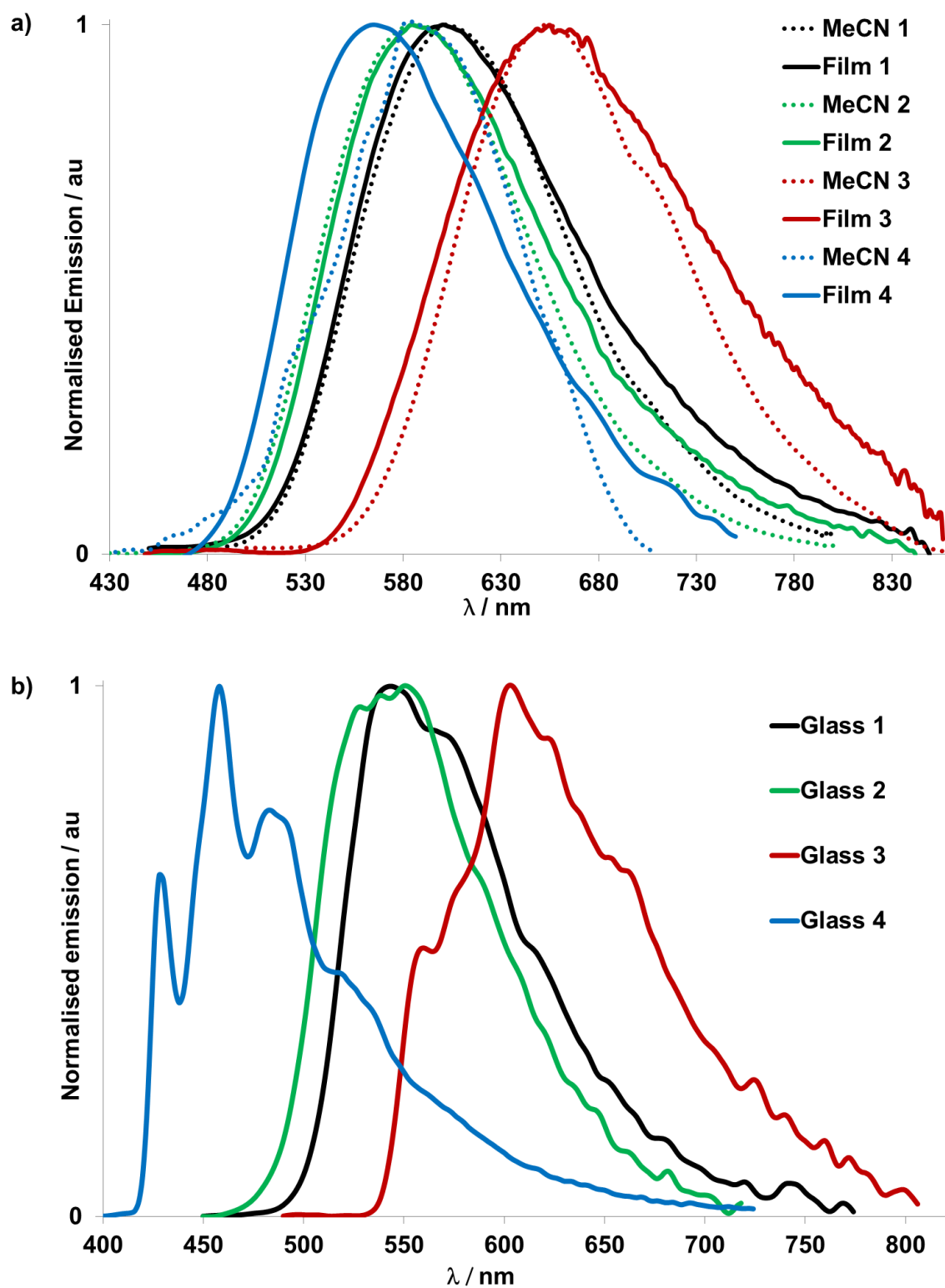


Figure 8. a) Photoluminescence spectra of complexes **1-4** recorded in MeCN (dotted lines) and PMMA doped films (5 wt% of complex in PMMA) in solid lines ($\lambda_{\text{exc}} = 420 \text{ nm}$ for **1-3** and $\lambda_{\text{exc}} = 400 \text{ nm}$ for **4**). b) Photoluminescence spectra of complexes **1-4** recorded in 2-MeTHF at 77 K. $\lambda_{\text{exc}} = 420 \text{ nm}$ for complexes **1-3** and $\lambda_{\text{exc}} = 380 \text{ nm}$ for **4**.

The low-intensity emission spectra at 77 K in 2-MeTHF glasses of **1-4** are noisy. Figure **8b** shows the smoothed emission profiles. A significant hypsochromic shift is observed compared to the measurements at 298 K, both in MeCN and as doped films. For instance, the profile for complex **1** shows an emission maximum at 544 nm and a shoulder at 572 nm resulting in a blue shift of 58 nm (900 cm^{-1}) for the $E_{0,0}$ peak compared to the spectrum in MeCN at 298 K with almost no shift compared to the emission of **R1** in the 2-MeTHF glass ($\lambda_{\text{PL}} = 542\text{ nm}$). The blue shift is less pronounced for **2** (33 nm, 1022 cm^{-1}), with peaks at 528, 552 and 536 ($\lambda_{\text{max}} = 552\text{ nm}$). However, compared to **R2** the highest intensity emission peak of complex **2** shows a significant red shift of 79 nm (3026 cm^{-1}). For complex **3** the normalized profile is centered at 604 nm (blue shift of 51 nm, 1289 cm^{-1} compared to the spectrum in MeCN). Complex **4** ($\lambda_{\text{exc}} = 380\text{ nm}$) is also very poorly emissive and the profile shows two moderately intense bands at 428 nm and 484 nm (and a shoulder at 534 nm) and the λ_{PL} located at 458 nm shows significant blue shift compared to the spectrum in MeCN (122 nm, 4593 cm^{-1}). The monoexponential emission lifetimes at 77 K in the microsecond regime are significantly longer compared to both sets of room-temperature measurements and range from 2088 ns (**1**), to 2120 ns (**2**), to 2363 ns (**3**) and 4423 ns (**4**). Compared to the reported emission lifetimes at 77 K of **R1** (4770 ns) and **R2** (4550 ns),¹⁵ **1** and **2** show significantly shorter lifetimes.

Table 4. Photophysical properties of **1-4** and **R1-R4**

	MeCN ^a			Film ^b			Glass ^c			
	$\lambda_{\text{PL}}^{\text{d}}$ / nm	$\Phi_{\text{PL}}^{\text{e}}$ / %	$\tau_{\text{PL}}^{\text{f}}$ / ns	$\lambda_{\text{PL}}^{\text{d}}$ / nm	$\Phi_{\text{PL}}^{\text{g}}$ / %	$\tau_{\text{PL}}^{\text{f}}$ / ns	$\lambda_{\text{PL}}^{\text{d}}$ / nm	$\tau_{\text{PL}}^{\text{f}}$ / ns	k_{r}^{h} $\times 10^{-5} / \text{s}^{-1}$	k_{nr}^{i} $\times 10^{-5} / \text{s}^{-1}$
1			26 (25%)			124 (11%)				
			110 (60%)			316 (56%)				
	602	3	346 (15%)	600	15	646 (33%)	544, 572 (sh)	2088	2.41	77.97
			Average			Average				
			124			404				
2			52 (29%)			99 (4%)				
			215 (58%)			318 (43%)	528, 536,			
	585	8	1038 (13%)	584	21	695 (53%)	552	2120	2.91	33.49
			Average			Average				
			275			509				
3			54 (79%)			93 (16%)				
			95 (19%)			254 (57%)				
	655	3	532 (2%)	655	7	605 (27%)	604	2363	4.20	135.95
			Average			Average				
			71			323				
4			17 (3%)			49 (2%)				
			131 (60%)			361 (23%)	428, 458,			
	580 ^j	0.5	420 (37%)	565 ⁱ	1	1482 (75%)	484, 534 (sh) ^k	4423	0.21	42.43
			Average			Average				
			235			1196				
R1^l	602	9	275	-		542	4770 ^m	3.4	33	

R2^l	591	27	386	-	473	4550 ^m	7.0	19
R3ⁿ	658	2	81	-	-	-	2.12	121.33
			361 (27%)					
	489,		720 (51%)					
R4	512	66	1761 (22%)	-	-	-	7.75	3.99
	(sh)		Average					
			852					

^a In deaerated MeCN at 298 K; ^b at 298 K, spin-coated from a 2-methoxyethanol solution of 5 wt% of the complex in PMMA on a pristine quartz substrate; ^c in 2-MeTHF at 77 K, if not specified differently; ^d λ_{exc} = 420 nm, if not specified differently; ^e [Ru(bpy)₃](PF₆)₂ in MeCN as reference (Φ_{PL} = 1.8% in aerated MeCN at 298 K)³⁵; ^f λ_{exc} = 378 nm, average weighted lifetimes were determined according to equation $\tau_{PL,avg} = \sum A_i \tau_i$ (A_i = pre-exponential factor of the *i*th lifetime τ_i); ^g Measured using an integrating sphere; ^h $k_r = \Phi_{PL,MeCN} / \tau_{PL}$; ⁱ $k_{nr} = [(1 - \Phi_{PL,MeCN}) / \tau_{PL}]$; ^j λ_{exc} = 400 nm; ^k λ_{exc} = 380 nm; ^l from ref ¹⁵; ^m Measured in 1/1 MeOH/EtOH glass state at 77 K; ⁿ from ref ²⁴.

Conclusions

A new series of four cationic Ir(III) complexes bearing nonconjugated C^N ligands, using the bpy ligand for the first time in luminescent Ir(III) complexes, have been synthesized and fully characterized. Comparative studies with the related series of ppy-based complexes show the impact of the methylene spacer present within the cyclometalated ligand on the electrochemical and photophysical properties. Analysis of the X-ray crystal structures for three of the complexes clearly illustrates the existence of two possible conformations. Depending on the nature of the ancillary ligand, phosphorescence ranging from yellow to deep red is observed in MeCN as well as in 5 wt% PMMA doped films. Variable-temperature ¹H and 2D ROESY-NMR studies show the presence of two conformers for complex **3** as a result of the fluxional behavior of the bridging methylene group of the cyclometalated bpy ligand, which is

consistent with DFT calculations yielding a small free energy difference but a rather large barrier to interconversion between the two conformers. DFT calculations suggest that the transition from one conformation to the other is a concerted process in which the two ligands simultaneously change their conformation. A similar behavior is observed **4**, but for this complex the major conformer is the opposite to the one observed for **3**. Under the same conditions, however, complexes **1** and **2** only show one conformer in the ^1H NMR at room temperature. All four complexes show quasi-reversible oxidation waves. Complexes **1-3** show quasi-reversible reduction waves while no reduction wave was detected within the solvent window for **4**. Compared to their reference complexes **R1-R4**, **1-4** emit at similar energies but show much lower photoluminescence quantum yields and shorter emission lifetimes. DFT calculations predict that conformer b is the most stable in the triplet state for **1-4**. Breaking the conjugation of the C \wedge N ligands did not change the triplet energy of the complexes despite reducing the electrochemical gap. This detailed joint theoretical and experimental study provides a better understanding of the role of the methylene spacer in the 2-benzylpyridinato cyclometalating ligands within this new series of Ir(III) complexes.

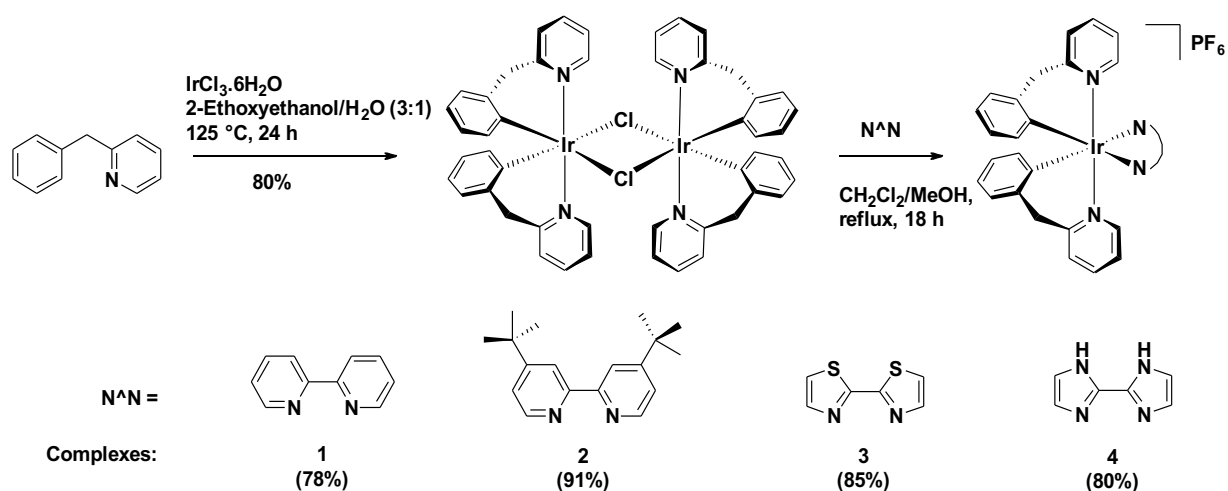
Experimental Section

General Synthetic Procedures

Commercial chemicals were used as supplied. All reactions were performed using standard Schlenk techniques under inert (N_2) atmosphere with reagent-grade solvents. Flash column chromatography was performed using silica gel (Silia-P from Silicycle, 60 Å, 40-63 μm). Analytical thin layer chromatography (TLC) was performed with silica plates with aluminum backings (250 μm with indicator F-254). Compounds were visualized under UV light. ^1H , ^{13}C and ^{31}P solution-phase NMR spectra were recorded on a Bruker Avance spectrometer operating at 11.7 T (Larmor frequencies of 500, 400, 126 and 162 MHz, respectively). The following abbreviations have been used for multiplicity assignments: “s” for singlet, “d” for doublet, “t”

for triplet and “m” for multiplet. ^1H and ^{13}C NMR spectra were referenced to the solvent peak. Melting points (Mps) were recorded using open-ended capillaries on an electrothermal melting point apparatus and are uncorrected. High-resolution mass spectra were recorded at the EPSRC UK National Mass Spectrometry Facility at Swansea University on a quadrupole time-of-flight (ESI-Q-TOF), model ABSciex 5600 Triple TOF in positive electrospray ionization mode and spectra were recorded using sodium formate solution as the calibrant. Elemental analyses were performed by Mr. Stephen Boyer, London Metropolitan University.

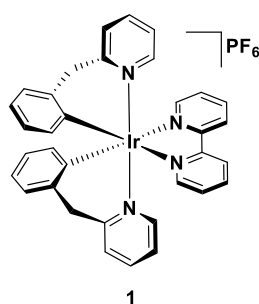
General procedure for the Synthesis of target Complexes 1-4



The $\text{IrCl}_3 \cdot 6\text{H}_2\text{O}$ (2.0 equiv.) and 2-benzylpyridine (5.0 equiv.) were suspended in a mixture of 2-ethoxyethanol/water (3:1). The mixture was heated and kept at 125°C under stirring. After 24 h the mixture was allowed to cool to r.t. and distilled water was added. A precipitate was observed. It was washed with Et_2O , H_2O and dried under vacuum to give the intermediate bis(μ -Cl) dimer complex. A suspension of this dimer (1.0 equiv.), the corresponding ancillary ligand (2.2 equiv.) in a mixture of CH_2Cl_2 /methanol (1:1) was degassed for 15 min and then heated and kept at reflux for 18 h under stirring. The solvent was then evaporated leaving a residue, which was purified over silica with dichloromethane and increasing percentages of methanol (0% - 8%). The desired fractions were collected and reduced till dryness, giving a solid that

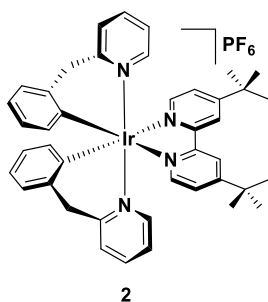
was then dissolved in methanol. An aqueous NH_4PF_6 solution was added dropwise resulting in a precipitate. The suspension was stirred vigorously for 2 h and subsequently filtered. The solid was dissolved in CH_2Cl_2 and washed with water. The layers were separated, and the organic layer was reduced till dryness leaving a solid, which was recrystallized through vapor diffusion using CH_2Cl_2 as solvent and Et_2O as precipitant. After filtration, the target complexes were obtained as solids.

Complex 1



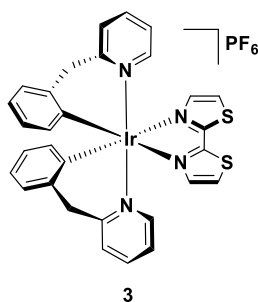
Red solid. **Yield:** 78%. **Mp.:** 244 – 248 °C. **^1H NMR (500 MHz, CDCl_3) δ (ppm):** 9.01 (d, $J = 8.2$ Hz, 2H), 8.32 (d, $J = 5.4$ Hz, 2H), 8.25 (td, $J = 7.9, 1.6$ Hz, 2H), 7.64 (s, 4H), 7.38 (t, $J = 6.6$ Hz, 2H), 7.32 (s, 2H), 7.00 (s, 4H), 6.92 (t, $J = 6.5$ Hz, 2H), 6.87 (t, $J = 6.6$ Hz, 2H), 6.61 (d, $J = 7.6$ Hz, 2H), 3.93 (d, $J = 15.6$ Hz, 2H), 3.56 (d, $J = 15.7$ Hz, 2H). **^{13}C NMR (126 MHz, CDCl_3) δ (ppm):** 163.39, 155.98, 150.88, 150.64, 139.77, 139.26, 138.32, 136.54, 135.87, 127.33, 127.07, 127.02, 126.90, 126.11, 123.88, 123.31, 49.18. **^{31}P NMR (162 MHz, CDCl_3) δ (ppm):** -144.34. **HR-MS (FTMS⁺):** $[\text{M}]^+$ **Calculated:** ($\text{C}_{34}\text{H}_{28}\text{IrN}_4$): 685.1939; **Found:** 685.1936. **CHN: Calcd for ($\text{C}_{34}\text{H}_{28}\text{F}_6\text{IrN}_4\text{P}$):** C, 49.21; H, 3.40; N, 6.75 **Found:** C, 49.06; H, 3.28; N, 6.68.

Complex 2



Yellow solid. **Yield:** 91%. **Mp.:** 252-257 °C. **¹H NMR (500 MHz, CDCl₃) δ (ppm):** 8.84 – 8.75 (m, 2H), 8.15 (d, *J* = 5.9 Hz, 2H), 7.71 (d, *J* = 7.0 Hz, 2H), 7.57 (td, *J* = 7.6, 1.4 Hz, 2H), 7.31 (dd, *J* = 5.9, 1.7 Hz, 2H), 7.25 (m, 2H), 7.03 – 6.89 (m, 6H), 6.82 (td, *J* = 7.6, 2.9 Hz, 2H), 6.61 (d, *J* = 7.3 Hz, 2H), 3.92 (d, *J* = 15.5 Hz, 2H), 3.51 (d, *J* = 15.5 Hz, 2H), 1.48 (s, 18H). **¹³C NMR (126 MHz, CDCl₃) δ (ppm):** 163.98, 163.19, 156.06, 151.28, 150.02, 139.45, 138.09, 137.40, 136.02, 126.81, 126.58, 125.89, 124.70, 123.93, 123.66, 122.96, 49.29, 35.88, 30.30. **³¹P NMR (162 MHz, CDCl₃) δ (ppm):** -142.42. **HR-MS (FTMS⁺): [M]⁺ Calculated:** (C₄₂H₄₄IrN₄): 797.3192; **Found:** 797.3188. **CHN: Calcd.** for C₄₂H₄₄F₆IrN₄P · ½ CH₂Cl₂: C, 51.85; H, 4.61; N, 5.96. **Found:** C, 51.89; H 4.28; N 5.51.

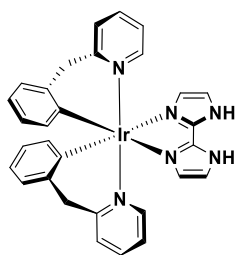
Complex 3



Deep red solid. **Yield:** 85%. **Mp.:** 235 °C (decomp.). **¹H NMR (500 MHz, CDCl₃) δ (ppm):** 8.14 (d, *J* = 3.3 Hz, 2H), 8.05 (d, *J* = 3.3 Hz, 2H), 7.99 (d, *J* = 5.4 Hz, 2H), 7.86 (d, *J* = 3.3 Hz, 2H), 7.65 – 7.57 (m, 6H), 7.55 (d, *J* = 6.0 Hz, 2H), 7.38 (d, *J* = 7.3 Hz, 2H), 7.28 (d, *J* = 7.4 Hz, 2H), 7.22 (d, *J* = 7.4 Hz, 2H), 7.02 (t, *J* = 6.2 Hz, 2H), 6.99 – 6.88 (m, 6H), 6.81 (dt, *J* = 14.1, 7.2 Hz, 4H), 6.59 (d, *J* = 7.4 Hz, 2H), 6.53 (t, *J* = 7.1 Hz, 2H), 5.39 (d, *J* = 7.7 Hz, 2H), 4.51

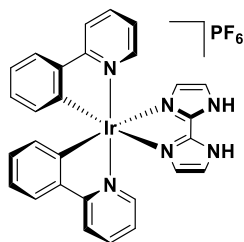
(d, $J = 16.2$ Hz, 2H), 4.13 (d, $J = 16.3$ Hz, 2H), 3.87 (d, $J = 15.4$ Hz, 2H), 3.52 (d, $J = 15.5$ Hz, 2H). ^{13}C NMR (126 MHz, CDCl_3) δ (ppm): 163.55, 163.49, 162.51, 161.39, 155.44, 150.43, 143.21, 142.68, 140.36, 139.31, 138.67, 138.35, 136.86, 136.63, 135.41, 132.69, 126.86, 126.71, 126.58, 126.45, 126.28, 126.03, 125.99, 125.04, 123.98, 123.46, 123.41, 53.59, 49.11, 48.41. ^{31}P NMR (162 MHz, CDCl_3) δ (ppm): -144.41. HR-MS (FTMS⁺): [M]⁺ Calculated: ($\text{C}_{30}\text{H}_{24}\text{IrN}_4\text{S}_2$): 697.1067; Found: 697.1049. CHN: Calcd. for $\text{C}_{30}\text{H}_{24}\text{F}_6\text{IrN}_4\text{PS}_2$: C, 42.80; H, 2.87; N, 6.66. Found: C, 42.43; H 2.82; N 6.55. The NMR data correspond to the mixture of **3a** and **3b** at 298 K.

Complex 4



Beige solid. Yield: 80%. Mp.: 259 °C (decomp.). ^1H NMR (400 MHz, CDCl_3) δ (ppm): 8.13 (d, $J = 6.9$ Hz, 2H), 7.59 (td, $J = 7.6, 1.5$ Hz, 2H), 7.36 – 7.32 (m, 3H), 7.24 (s, 2H), 7.17 (d, $J = 7.7$ Hz, 2H), 6.95 – 6.84 (m, 3H), 6.80 – 6.74 (m, 2H), 6.53 (t, $J = 7.4$ Hz, 2H), 5.43 (d, $J = 8.7$ Hz, 2H), 4.73 (d, $J = 16.3$ Hz, 2H), 4.04 (d, $J = 16.0$ Hz, 2H). ^{13}C NMR (126 MHz, CDCl_3) δ (ppm): 162.82, 156.23, 141.86, 140.51, 138.47, 137.85, 137.74, 128.59, 126.13, 125.84, 124.40, 122.88, 122.50, 120.15, 48.54. ^{31}P NMR (162 MHz, CDCl_3) δ (ppm): -143.81. HR-MS (FTMS⁺): [M]⁺ Calculated: ($\text{C}_{30}\text{H}_{26}\text{IrN}_6$) 663.1844; Found: 663.1834. The NMR data correspond only to the major conformer **4a**.

Complex R4



Complex **R4** was obtained according the general procedure using 2-phenylpyridine instead of 2-benzylpyridine. Beige solid. **Yield:** 80%. **Mp.:** 259 °C (decomp.). **¹H NMR (400 MHz, CDCl₃) δ (ppm):** 12.01 (s, 2H), 8.01 (d, J = 8.1 Hz, 2H), 7.84 – 7.78 (m, 2H), 7.78 – 7.68 (m, 4H), 7.25 (d, J = 1.5 Hz, 2H), 7.07 (ddd, J = 7.4, 5.8, 1.4 Hz, 2H), 6.99 – 6.93 (m, 2H), 6.83 (td, J = 7.4, 1.4 Hz, 2H), 6.47 (d, J = 1.5 Hz, 2H), 6.33 (dd, J = 7.6, 1.2 Hz, 2H). **¹³C NMR (126 MHz, CDCl₃) δ (ppm):** 168.73, 150.44, 149.61, 145.52, 141.34, 138.78, 132.72, 130.45, 127.88, 125.18, 123.98, 122.59, 121.60, 120.00. **HR-MS (FTMS⁺): [M]⁺ Calculated:** (C₃₀H₂₆IrN₆) 635.1531; **Found:** 653.1517. **CHN: Calcd.** for C₂₈H₂₂F₆IrN₆P: C, 43.13; H, 2.84; N, 10.78. **Found:** C, 43.16; H 2.91; N 10.83. The crystal structure obtained is of the chloride salt, denoted as **R4.Cl**.

Acknowledgment

We thank Umicore AG for the gift of materials. We thank the EPSRC UK National Mass Spectrometry Facility at Swansea University for analytical services. C.H. acknowledges the *Région Bretagne*, France for funding. D.J. acknowledges the European Research Council and the *Région des Pays de la Loire* for financial support in the framework of a Starting Grant (Marches - 278845) and the LUMOMAT RFI project, respectively. This research used resources of 1) the GENCI-CINES/IDRIS, 2) the CCIPL (*Centre de Calcul Intensif des Pays de Loire*), 3) a local Troy cluster. E.Z.-C. acknowledges the University of St. Andrews and EPSRC (EP/M02105X/1) for financial support.

Supporting information. CIF files for the X-ray structures of **1-3** and **R4** (CCDC: 1584175-1584178). NMR and mass spectra for **1-4**, **R4**, Supplementary crystallographic,

electrochemical and photophysical data. Description of the computational protocol and supplementary computational results including a movie of the transition state connecting **3a** and **3b**.

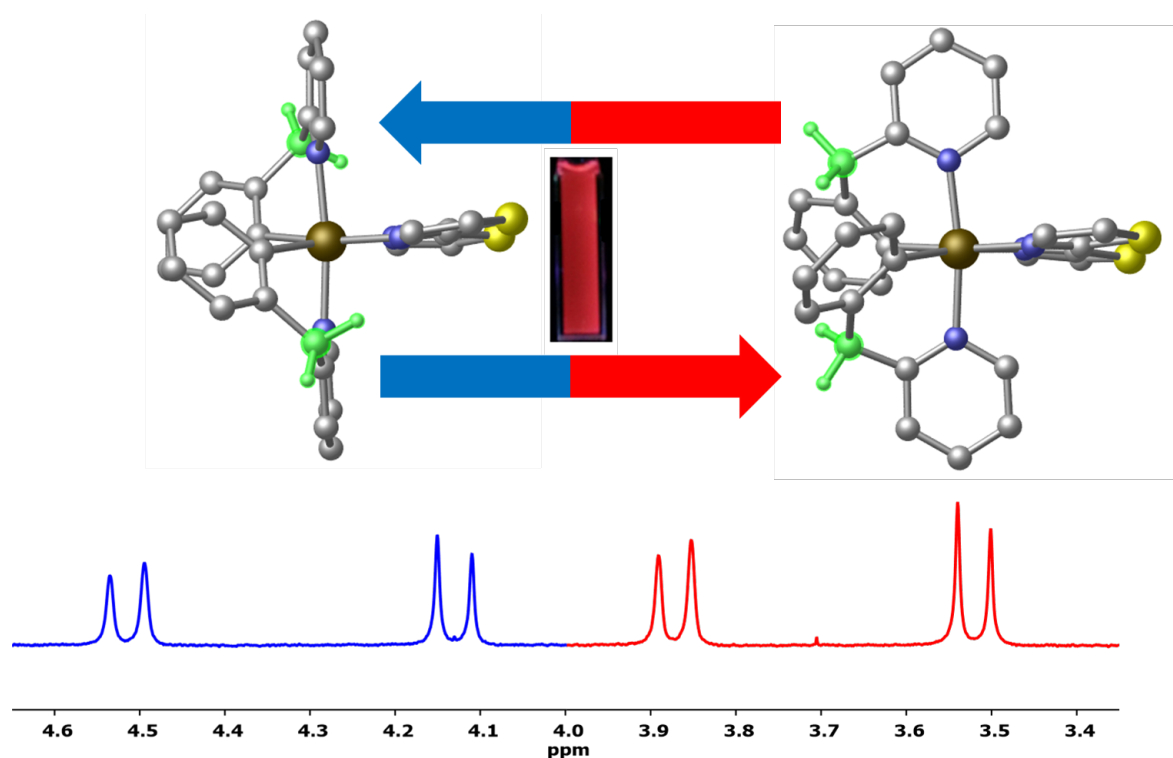
References

- (1) Henwood, A. F.; Zysman-Colman, E., Lessons learned in tuning the optoelectronic properties of phosphorescent iridium(III) complexes. *Chem. Commun.* **2017**, 53, 807.
- (2) Zannoni, K. P. S.; Coppo, R. L.; Amaral, R. C.; Murakami Iha, N. Y., Ir(III) complexes designed for light-emitting devices: beyond the luminescence color array. *Dalton Trans.* **2015**, 44, 14559.
- (3) Ladouceur, S.; Zysman-Colman, E., A Comprehensive Survey of Cationic Iridium(III) Complexes Bearing Nontraditional Ligand Chelation Motifs. *Eur. J. Inorg. Chem.* **2013**, 2013, 2985.
- (4) Terki, R.; Simoneau, L.-P.; Rochefort, A., Tailoring the Photoluminescence Properties of Ionic Iridium Complexes. *J. Phys. Chem. A* **2009**, 113, 534.
- (5) Lu, C. W.; Wang, Y.; Chi, Y., Metal Complexes with Azolate-Functionalized Multidentate Ligands: Tactical Designs and Optoelectronic Applications. *Chemistry* **2016**, 22, 17892.
- (6) Li, H.-C.; Chou, P.-T.; Hu, Y.-H.; Cheng, Y.-M.; Liu, R.-S., Synthesis, Characterization, and Photophysical Properties of Iridium Complexes with an 8-Phenylquinoline Framework. The First Six-Membered Chelated Iridium Complexes for Electroluminescence. *Organometallics* **2005**, 24, 1329.
- (7) Zhu, R.; Lin, J.; Wen, G.-A.; Liu, S.-J.; Wan, J.-H.; Feng, J.-C.; Fan, Q.-L.; Zhong, G.-Y.; Wei, W.; Huang, W., Color Tuning Based on a Six-membered Chelated Iridium(III) Complex with Aza-aromatic Ligand. *Chem. Lett.* **2005**, 34, 1668.
- (8) Thamilarasan, V.; Jayamani, A.; Manisankar, P.; Kim, Y.-I.; Sengottuvelan, N., Green-emitting phosphorescent iridium(III) complex: Structural, photophysical and electrochemical properties. *Inorg. Chim. Acta* **2013**, 408, 240.
- (9) Song, Y. H.; Chiu, Y. C.; Chi, Y.; Cheng, Y. M.; Lai, C. H.; Chou, P. T.; Wong, K. T.; Tsai, M. H.; Wu, C. C., Phosphorescent iridium(III) complexes with nonconjugated cyclometalated ligands. *Chem. Eur. J.* **2008**, 14, 5423.
- (10) Chang, C.-F.; Cheng, Y.-M.; Chi, Y.; Chiu, Y.-C.; Lin, C.-C.; Lee, G.-H.; Chou, P.-T.; Chen, C.-C.; Chang, C.-H.; Wu, C.-C., Highly Efficient Blue-Emitting Iridium(III) Carbene Complexes and Phosphorescent OLEDs. *Angew. Chem. Int. Ed.* **2008**, 47, 4542.
- (11) Zhang, F.; Ma, D.; Duan, L.; Qiao, J.; Dong, G.; Wang, L.; Qiu, Y., Synthesis, characterization, and photophysical and electroluminescent properties of blue-emitting cationic iridium(III) complexes bearing nonconjugated ligands. *Inorg Chem* **2014**, 53, 6596.
- (12) Hierlinger, C.; Roisnel, T.; Cordes, D. B.; Slawin, A. M. Z.; Jacquemin, D.; Guerschais, V.; Zysman-Colman, E., An Unprecedented Family of Luminescent Iridium(III) Complexes Bearing a Six-Membered Chelated Tridentate C^NC Ligand. *Inorg Chem* **2017**, 56, 5182.
- (13) Li, L.; Brennessel, W. W.; Jones, W. D., C-H Activation of Phenyl Imines and 2-Phenylpyridines with [Cp*MC12]2 (M = Ir, Rh): Regioselectivity, Kinetics, and Mechanism. *Organometallics* **2009**, 28, 3492.

- (14) Boutadla, Y.; Davies, D. L.; Jones, R. C.; Singh, K., The scope of ambiphilic acetate-assisted cyclometallation with half-sandwich complexes of iridium, rhodium and ruthenium. *Chemistry* **2011**, *17*, 3438.
- (15) Ladouceur, S.; Fortin, D.; Zysman-Colman, E., Enhanced Luminescent Iridium(III) Complexes Bearing Aryltriazole Cyclometallated Ligands. *Inorg. Chem.* **2011**, *50*, 11514.
- (16) Donato, L.; Abel, P.; Zysman-Colman, E., Cationic iridium(III) complexes bearing a bis(triazole) ancillary ligand. *Dalton Trans.* **2013**, *42*, 8402.
- (17) Fernandez-Hernandez, J. M.; Ladouceur, S.; Shen, Y.; Iordache, A.; Wang, X.; Donato, L.; Gallagher-Duval, S.; de Anda Villa, M.; Slinker, J. D.; De Cola, L.; Zysman-Colman, E., Blue light emitting electrochemical cells incorporating triazole-based luminophores. *J. Mater. Chem. C* **2013**, *1*, 7440.
- (18) Ladouceur, S.; Swanick, K. N.; Gallagher-Duval, S.; Ding, Z.; Zysman-Colman, E., Strongly Blue Luminescent Cationic Iridium(III) Complexes with an Electron-Rich Ancillary Ligand: Evaluation of Their Optoelectronic and Electrochemiluminescence Properties. *Eur. J. Inorg. Chem.* **2013**, *2013*, 5329.
- (19) Evariste, S.; Sandroni, M.; Rees, T. W.; Roldan-Carmona, C.; Gil-Escrig, L.; Bolink, H. J.; Baranoff, E.; Zysman-Colman, E., Fluorine-free blue-green emitters for light-emitting electrochemical cells. *J. Mater. Chem. C* **2014**, *2*, 5793.
- (20) Henwood, A. F.; Evariste, S.; Slawin, A. M. Z.; Zysman-Colman, E., Rigid biimidazole ancillary ligands as an avenue to bright deep blue cationic iridium(III) complexes. *Faraday Discuss.* **2014**, *174*, 165.
- (21) Shavaleev, N. M.; Xie, G.; Varghese, S.; Cordes, D. B.; Slawin, A. M. Z.; Momblona, C.; Ortí, E.; Bolink, H. J.; Samuel, I. D. W.; Zysman-Colman, E., Green Phosphorescence and Electroluminescence of Sulfur Pentafluoride-Functionalized Cationic Iridium(III) Complexes. *Inorg. Chem.* **2015**, *54*, 5907.
- (22) Henwood, A. F.; Bansal, A. K.; Cordes, D. B.; Slawin, A. M. Z.; Samuel, I. D. W.; Zysman-Colman, E., Solubilised bright blue-emitting iridium complexes for solution processed OLEDs. *J. Mater. Chem. C* **2016**, *4*, 3726.
- (23) Rota Martir, D.; Bansal, A. K.; Di Mascio, V.; Cordes, D. B.; Henwood, A. F.; Slawin, A. M. Z.; Kamer, P. C. J.; Martinez-Sarti, L.; Pertegas, A.; Bolink, H. J.; Samuel, I. D. W.; Zysman-Colman, E., Enhancing the photoluminescence quantum yields of blue-emitting cationic iridium(III) complexes bearing bisphosphine ligands. *Inorganic Chemistry Frontiers* **2016**, *3*, 218.
- (24) Pal, A. K.; Cordes, D. B.; Slawin, A. M. Z.; Momblona, C.; Pertegas, A.; Orti, E.; Bolink, H. J.; Zysman-Colman, E., Simple design to achieve red-to-near-infrared emissive cationic Ir(III) emitters and their use in light emitting electrochemical cells. *RSC Advances* **2017**, *7*, 31833.
- (25) Nonoyama, M., Benzo[h]quinolin-10-yl-N Iridium(III) Complexes. *Bull. Chem. Soc. Jpn.* **1974**, *47*, 767.
- (26) Henwood, A. F.; Zysman-Colman, E. In *Iridium(III) in Optoelectronic and Photonics Applications*; John Wiley & Sons, Ltd: **2017**, 275.
- (27) Costa, R. D.; Ortí, E.; Bolink, H. J.; Graber, S.; Schaffner, S.; Neuburger, M.; Housecroft, C. E.; Constable, E. C., Archetype Cationic Iridium Complexes and Their Use in Solid-State Light-Emitting Electrochemical Cells. *Adv. Funct. Mater.* **2009**, *19*, 3456.
- (28) Martir, D. R.; Momblona, C.; Pertegás, A.; Cordes, D. B.; Slawin, A. M. Z.; Bolink, H. J.; Zysman-Colman, E., Chiral Iridium(III) Complexes in Light-Emitting Electrochemical Cells: Exploring the Impact of Stereochemistry on the Photophysical Properties and Device Performances. *ACS Applied Materials & Interfaces* **2016**, *8*, 33907.
- (29) Pavlishchuk, V. V.; Addison, A. W., Conversion constants for redox potentials measured versus different reference electrodes in acetonitrile solutions at 25°C. *Inorg. Chim. Acta* **2000**, *298*, 97.

- (30) Lowry, M. S.; Hudson, W. R.; Pascal Jr., R. A.; Bernhard, S., Accelerated Luminophore Discovery through Combinatorial Synthesis. *J. Am. Chem. Soc.* **2004**, *126*, 14129.
- (31) Cardona, C. M.; Li, W.; Kaifer, A. E.; Stockdale, D.; Bazan, G. C., Electrochemical Considerations for Determining Absolute Frontier Orbital Energy Levels of Conjugated Polymers for Solar Cell Applications. *Adv. Mater.* **2011**, *23*, 2367.
- (32) Gärtner, F.; Cozzula, D.; Losse, S.; Boddien, A.; Anilkumar, G.; Junge, H.; Schulz, T.; Marquet, N.; Spannenberg, A.; Gladiali, S.; Beller, M., Synthesis, Characterisation and Application of Iridium(III) Photosensitisers for Catalytic Water Reduction. *Chem. Eur. J.* **2011**, *17*, 6998.
- (33) Ertl, C. D.; Momblona, C.; Pertegás, A.; Junquera-Hernández, J. M.; La-Placa, M.-G.; Prescimone, A.; Ortí, E.; Housecroft, C. E.; Constable, E. C.; Bolink, H. J., Highly Stable Red-Light-Emitting Electrochemical Cells. *J. Am. Chem. Soc.* **2017**, *139*, 3237.
- (34) For examples see: Ladouceur, S.; Fortin, D.; Zysman-Colman, E., Enhanced Luminescent Iridium(III) Complexes Bearing Aryltriazole Cyclometallated Ligands. *Inorg. Chem.* **2011**, *50*, 11514
- (35) Suzuki, K.; Kobayashi, A.; Kaneko, S.; Takehira, K.; Yoshihara, T.; Ishida, H.; Shiina, Y.; Oishi, S.; Tobita, S., Reevaluation of absolute luminescence quantum yields of standard solutions using a spectrometer with an integrating sphere and a back-thinned CCD detector. *Phys Chem Chem Phys* **2009**, *11*, 9850.

TOC



Synopsis. A new series of cationic iridium(III) complexes with nonconjugated benzylpyridinato as cyclometalating ligands has been prepared. The methylene spacer in the C[^]N ligand provides conformational flexibility leading to the formation of two conformers.

NMR studies and detailed density functional theory (DFT) studies show how the fluxional behavior is influenced by the choice of the ancillary ligand.